Acta Materialia 167 (2019) 275–286

Contents lists available at ScienceDirect

Acta Materialia

journal homepage: www.elsevier.com/locate/actamat

Full length article

Design of $D0_{22}$ superlattice with superior strengthening effect in high entropy alloys

Feng He [a, b, 1], Da Chen [b, 1], Bin Han [b], Qingfeng Wu [a], Zhijun Wang [a, *], Shaolou Wei [c], Daixiu Wei [d], Jincheng Wang [a, **], C.T. Liu [b], Ji-jung Kai [b, e, ***]

[a] State Key Laboratory of Solidification Processing, Northwestern Polytechnical University, Xi'an, 710072, PR China
[b] Department of Mechanical and Biomedical Engineering, City University of Hong Kong, Hong Kong, China
[c] Department of Materials Science and Engineering, Massachusetts Institute of Technology, Cambridge, MA, 02139, USA
[d] Institute for Materials Research, Tohoku University, 2-1-1 Katahira, Sendai, Miyagi, 980-8577, Japan
[e] Centre for Advanced Nuclear Safety and Sustainable Development, City University of Hong Kong, Hong Kong, China

ARTICLE INFO

Article history:
Received 20 November 2018
Received in revised form
24 January 2019
Accepted 27 January 2019
Available online 4 February 2019

Keywords:
High entropy alloys
Alloy design
$D0_{22}$ superlattice
Precipitation strengthening

ABSTRACT

Precipitation strengthening is one of the most promising mechanisms to develop high-performance high entropy alloys (HEAs). However, the design of a reinforcing phase with an excellent strengthening effect is still one of the most pivotal challenges. In the present study, a design strategy based on overall valence electron concentration (OVEC) is developed, and a coherent $D0_{22}$ superlattice (noted as γ'' phase) with superior strengthening effect is designed. The newly developed γ'' phase is systematically characterized using transmission electron microscope and atom probe tomography. Differentiating from the traditional Ni_3Nb γ'' phase, the present high-entropy γ'' phase contains ~7.7% Co and follows the $(Ni,Co,Cr,Fe)_3(Nb,Fe)$ stoichiometry. Three γ'' phase variants are observed with crystallographic orientation relationships of $[001]_{\gamma''}//<001>_{\gamma}$ and $(001)_{\gamma''}//\{100\}_{\gamma}$. The lenticular γ'' particles with small volume fraction (7%) causes a significant yield strength increase (670 MPa) and ductility retention (40%), resulting in excellent yield strength-ductility combination. The excellent strengthening effect of the γ'' phase is attributed to both ordering strengthening and coherency strengthening. The present study proposes a new design strategy of precipitates and develops a superior reinforcing phase for HEAs. These findings will not only promote the development of precipitation-hardened HEAs but deepen the fundamentals of precipitates design for other complex concentrated alloys as well.

1. Introduction

High entropy alloys (HEAs) with complex concentrated compositions have shown much simpler phase compositions than that predicted by the phase rule [1,2]. Particularly, three representative HEA systems exhibit single-phase solid solutions [3–5]. In the past decades, great efforts have been made to reveal the intriguing mechanical and physical properties of these complex-concentrated single-phase HEAs [6–10]. The face centered cubic (FCC) HEAs have been found to be very ductile and highly damage-tolerance [6,8]. Besides, FCC HEAs also showed promising functional properties, such as good irradiation and corrosion-resistance [11,12]. However, single-phase FCC HEAs were not strong enough for structural applications [13,14]. Strengthening the FCC HEAs have attracted broad scientific interests. Hereinto, one of the critical challenges is to efficiently strengthen FCC HEAs without a significant ductility sacrifice.

Several metallurgical mechanisms, including solid solution strengthening [15–18], defect engineering [19–23], and precipitation strengthening [24–26], have been applied to strengthen FCC HEAs. Precipitation-strengthening showed very promising advantages among the aforementioned strengthening mechanisms [24,27]. In the development of precipitation-hardened HEAs, two different types of precipitates have been developed. The coherent γ' phase with the $L1_2$ superlattice was firstly considered. Several groups have demonstrated that the γ' phase can be obtained by

* Corresponding author.
** Corresponding author.
*** Corresponding author. Department of Mechanical and Biomedical Engineering, City University of Hong Kong, Hong Kong, China.
E-mail addresses: zhjwang@nwpu.edu.cn (Z. Wang), jchwang@nwpu.edu.cn (J. Wang), jijkai@cityu.edu.hk (J.-j. Kai).
[1] These authors contribute equally to this work.

https://doi.org/10.1016/j.actamat.2019.01.048
1359-6454/

alloying Al and Ti [27–30]. The dominant strengthening mechanism of the γ′ phase is ordering strengthening since dislocations cut through the spherical particles and the lattice misfit between γ′ phase and matrix is very small [28,29]. Consequently, although the γ′ phase haven't caused severe ductility reduction, the yield strength increase is also modest. One possible method that further enhances the strength is to improve the volume fraction of γ′ phase [30,31]. However, increasing the Al and Ti concentration to increase the volume fraction of γ′ phase will lead to the formation of intermetallic compounds or other processing problems [27,30]. Apart from coherent γ′ particles, intermetallic particles with fully incoherent phase boundaries were also reported to be effective in strengthening FCC HEAs [32,33]. Liu et al. [32] demonstrated that the FCC HEAs possess extremely high work-hardening exponent and thus prevent the propagation of mirco-cracks between matrix and intermetallic particles. Their idea is that the high work hardening exponent leads to fast increase in strength during straining. The deformation level at the crack tip is higher than other areas around the crack, therefore, the strength of the crack tip is much higher than the other areas. Consequently, a higher stress is needed for the crack to propagate. Nevertheless, intermetallic particles strengthen HEAs through Orowan relation and thus result in good strength but bad ductility. Therefore, finding a new effective strengthening precipitate in HEAs is worthy of exploration. In superalloys, the γ″ phase is the most widely used precipitate except for γ′ phase [14]. The γ″ phase strengthens alloys through both ordering strengthening and coherency strengthening [34]. Besides, the γ″ phase usually has higher anti-phase boundary energy and higher lattice misfit than those of γ′ phase, resulting better strengthening effects [35]. However, designing γ″ for complex concentrated alloys is challenging and only a few very recent articles reported the γ″ of HEAs without demonstrating design principles [36].

In the present study, an overall valence electron concentration (OVEC) principle is proposed to design the precipitates in HEAs. Following this design strategy, a γ″ phase with $D0_{22}$ superlattice was introduced into the Co–Cr–Fe–Ni system. An excellent yield strength of ~954 MPa and elongation of ~28% were obtained in this γ″-bearing HEA. The crystallographic features and elemental partition of the γ″-bearing HEA were evaluated by transmission electron microscope (TEM), atom probe topography (APT). The mechanisms for the superior strengthening effect of γ″ phase has been discussed.

2. Designing $D0_{22}$ precipitates

An overall valence electron concentration (OVEC) principle is referenced for the design of the γ″ precipitate in the present study. The idea is inspired by the valence electron concentration (VEC) features of intermetallic alloys. Binary intermetallic alloys, such as Ni_3Mo, Ni_3V, Ni_3Ti and Ni_3Al, show $D0_a$, $D0_{22}$, $D0_{19}$, and $L1_2$ ordered structures. The upper side of Fig. 1(a) shows the VEC variation of typical intermetallic compounds and their crystallographic structures. Generally, the crystal structure transforms from the tetragonal to hexagonal and then to cubic structures with the decrease of VEC. Specifically, the tetragonal structure ($D0_a$ and $D0_{22}$) prefers higher VEC (>8.75), the hexagonal structure occurs when VEC is close to 8.5, and the $L1_2$ structure tends to form at lower VEC (<8.25). It shows that the main physical metallurgical parameter controlling these ordered intermetallic alloys is the VEC value. This simple rule can also be extended to complex concentrated alloys (CCAs). Liu et al. [37] found that the crystal structure of the complex concentrated $(Co,Ni,Fe)_3V$ alloys transform from tetragonal (8.75 < VEC) to purely cubic ordered structures (VEC<7.89) through an ordered hexagonal structures (7.89 < VEC<8.75). The effect of VEC on the crystal of HEAs is also investigated by Guo et al. [38]. In HEAs, the FCC phases are found to be stable at higher VEC (>8), and instead the body centered cubic (BCC) phases are stable at lower VEC (<6.87).

Applying the VEC principle from single-phase intermetallic alloys to the design of precipitates in a dual-phase alloys is challenging but intriguing. Recently, Yang et al. [39] demonstrated that the VEC of precipitates also effectively affects their crystal structures even in a dual-phase alloy system. However, it is extremely difficult to precisely measure or control the chemical compositions of precipitates. Therefore, we aim to design the precipitates by tuning the OVEC value of alloys by simply controlling the nominal compositions of the alloys. To validate whether the OVEC of alloys affects the crystal structure of precipitates or not, we overviewed CCAs strengthened by different precipitates, as shown in Table S1. The lower side of Fig. 1(a) shows the OVEC distribution of those precipitation-strengthened CCAs. To our amazement, the γ″ phase tends to precipitate in CCAs with OVEC higher than 8.4 while the γ′ phase prefers to occur in CCAs with OVEC lower than 8.4. Note that some γ″ and γ′ are metastable in many alloys and may transform into δ and η phases respectively upon aging. Comparing the chemical compositions of the CCAs with different precipitates (Table S1), we find that the most γ″-strengthened HEAs contain Nb, V, or Ta elements while most γ′-strengthened CCAs contain Al or Ti elements. This indicates that the Nb, V, and Ta are γ″ former and the Al and Ti are γ′ former, which can be explained from the crystal structure of the binary alloys. The Ni_3Al is stable with the $L1_2$ structure and the Ni_3Ti also has metastable form with the $L1_2$ structure. Similarly, the Ni_3V is stable in the $D0_{22}$ structure and both Ni_3Nb and Ni_3Ta can exist in a metastable form of the $D0_{22}$ structure. Accordingly, we design the γ″ precipitate in HEAs by following these two principles: a) making the OVEC of HEAs higher than 8.4; and b) adding the elements in group VB.

Following in the aforementioned design strategy, we design a $Ni_2CoCrFeNb_{0.15}$ HEA as a case study in the current work. The γ″ phase has been reported in a hypo-eutectic $CoCrFeNiNb_{0.25}$ HEA [40]. However, the $CoCrFeNiNb_{0.25}$ HEA consists of Nb-rich Laves phase and the γ″ transforms into a ε phase quickly. The appearance of the γ″ phase in the $CoCrFeNiNb_{0.25}$ HEA indicates that the Nb facilitates the formation of γ″ in the Co–Cr–Fe–Ni system, which is consistent with our design strategy. The OVEC of $CoCrFeNiNb_{0.25}$ HEA is 8.06, lower than the critical value of 8.4. To increase the OVEC of the Nb containing HEA, we increase the content of elements with a higher VEC (Ni in the present study) and decrease the content of elements with a lower VEC (mainly the Nb content in this work). Consequently, the $Ni_2CoCrFeNb_{0.15}$ HEA with OVEC of 8.495 is developed. To further confirm the design of γ″-bearing HEAs, The CALculation PHAse Diagram (CALPHAD) is also used to confirm the alloy design and to predict the precipitation behavior based on the JMatPro software with the TTNi8 database [7,31,41]. Fig. 1(b) shows the equilibrium phase diagram of the $Ni_2CoCrFeNb_{0.15}$ HEA, indicating a single FCC phase at high temperature and a single δ phase precipitation at low temperatures. Fig. 1(c) shows the calculated Temperature-Transformation-Time (TTT) diagram of the $Ni_2CoCrFeNb_{0.15}$ HEA. Clearly, the γ″ phase precipitates firstly from the FCC matrix and then transforms into the δ phase upon aging. In order to obtain the γ″ phase and suppress the δ and Laves phases, a relatively low annealing temperature of 650 °C is used in the present study to slow down the transformation kinetics.

3. Experimental details

Samples with the nominal composition of $Ni_2CoCrFeNb_{0.15}$ were prepared using arc melting and copper mold casting. Elements of

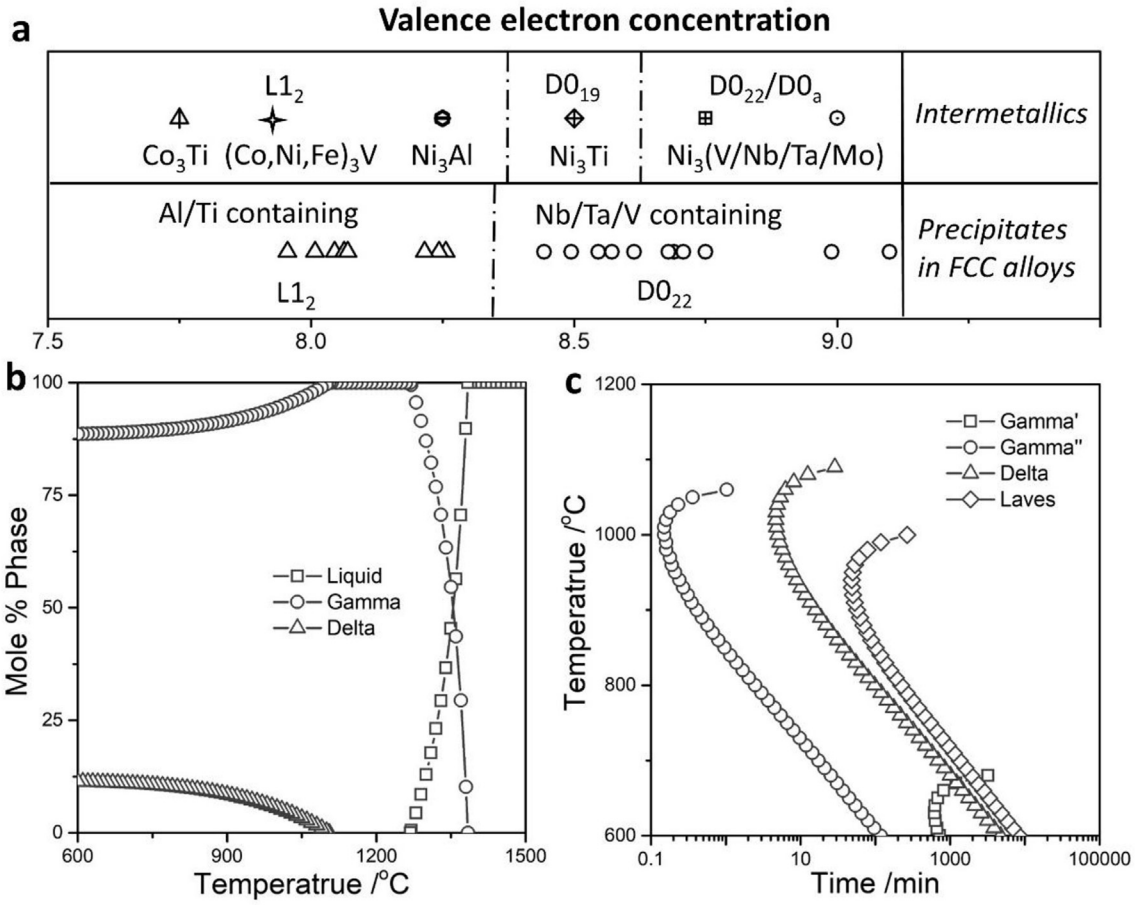

Fig. 1. (a) The evolution of crystal structures of intermetallic compounds and precipitates of CCAs with VEC/OVEC variations; (b) the equilibrium phase diagram of the $Ni_2CoCrFeNb_{0.15}$ HEA; and (c) the TTT diagram of the $Ni_2CoCrFeNb_{0.15}$ HEA. The calculation is carried out on JMatPro software with TTNi8 database.

Co, Cr, Fe, Ni and Nb with purity of 99.95% were used as raw materials. The alloys were melted for five times to ensure the homogeneity and then solidified in a water-cooled copper hearth with the dimension of $50 \times 10 \times 5\ mm^3$. The ingots were solid solution treated at 1200 °C for 2 h followed by water quenching to obtain single-phase HEAs. The solid solution treated HEAs were cold rolled to ~1.5 mm (~70% thickness reduction) and then recrystallized at 1200 °C for 4 min and finally quenched in water. To obtain the precipitates, the recrystallized HEAs were annealed at 650 °C for 80 h and 120 h.

The SEM samples were prepared by grinding, polishing in diamond suspension, and final polishing in colloidal silica suspension and then analyzed by scanning electron microscope (SEM SU6600). Transmission electron microscope (TEM JEOL 2100F) and X-Ray diffraction (XRD) were used to identify the crystal structure of the HEAs. For the TEM analysis, sheet samples with 0.5 mm in thickness were fist cut from the annealed samples by electrical discharged machining (EDM) and then mechanically ground to a thickness of ~70 μm using SiC papers. After that, the samples were punched into 3-mm-diameter discs and further thinned by ion-milling to a thickness of electron transparency. Atom probe tomography (APT) was used to identify the chemical compositions of nano-sized phases. Needle-shaped specimens required for APT were fabricated by lift-outs and annular milled in a FEI Scios focused ion beam/scanning electron microscope (FIB/SEM). The APT characterizations were performed in a local electrode atom probe (CAMEACA LEAP 5000 R). The APT specimens were tested at −223 °C in voltage mode, with a pulse repetition rate of 200 KHz, a pulse fraction of 20%, and an evaporation detection rate of 0.2% atom per pulse. Imago Visualization and Analysis Software (IVAS) in version 3.6.12 is used for 3D reconstruction and composition analysis.

For mechanical tests, dog-bone samples with gauge dimension of $12.5 \times 1.2 \times 3\ mm^3$ were used. Uniaxial tensile test was carried out on an Instron testing machine (INSTRON 3382) with a strain rate of $1 \times 10^{-3}\ s^{-1}$ at room temperature.

4. Results

4.1. XRD and SEM results

The XRD patterns and SEM images of $Ni_2CoCrFeNb_{0.15}$ HEAs at different annealing states are presented in Fig. 2. The XRD pattern of the solid-solution $Ni_2CoCrFeNb_{0.15}$ HEA in Fig. 2(a) is indexed to be a single FCC phase. The lattice parameter is calculated to be 3.587 Å, using the three strongest peaks. Fig. 2(b) shows typical single-phase recrystallized equiaxed grains with grain size of ~45 μm. A high magnification SEM image in Fig. 2(c) shows that there is no second phase inside the grain or at the grain boundaries. The small black dots are all inclusions, easily forming during solidification processes. Fig. 2(d)–(f) show the XRD pattern and microstructure of the $Ni_2CoCrFeNiNb_{0.15}$ HEA annealed at 650 °C for 80 h. The XRD result indicates a single FCC phase with a lattice parameter of $a_m = 3.585$ Å, while the high magnification SEM image

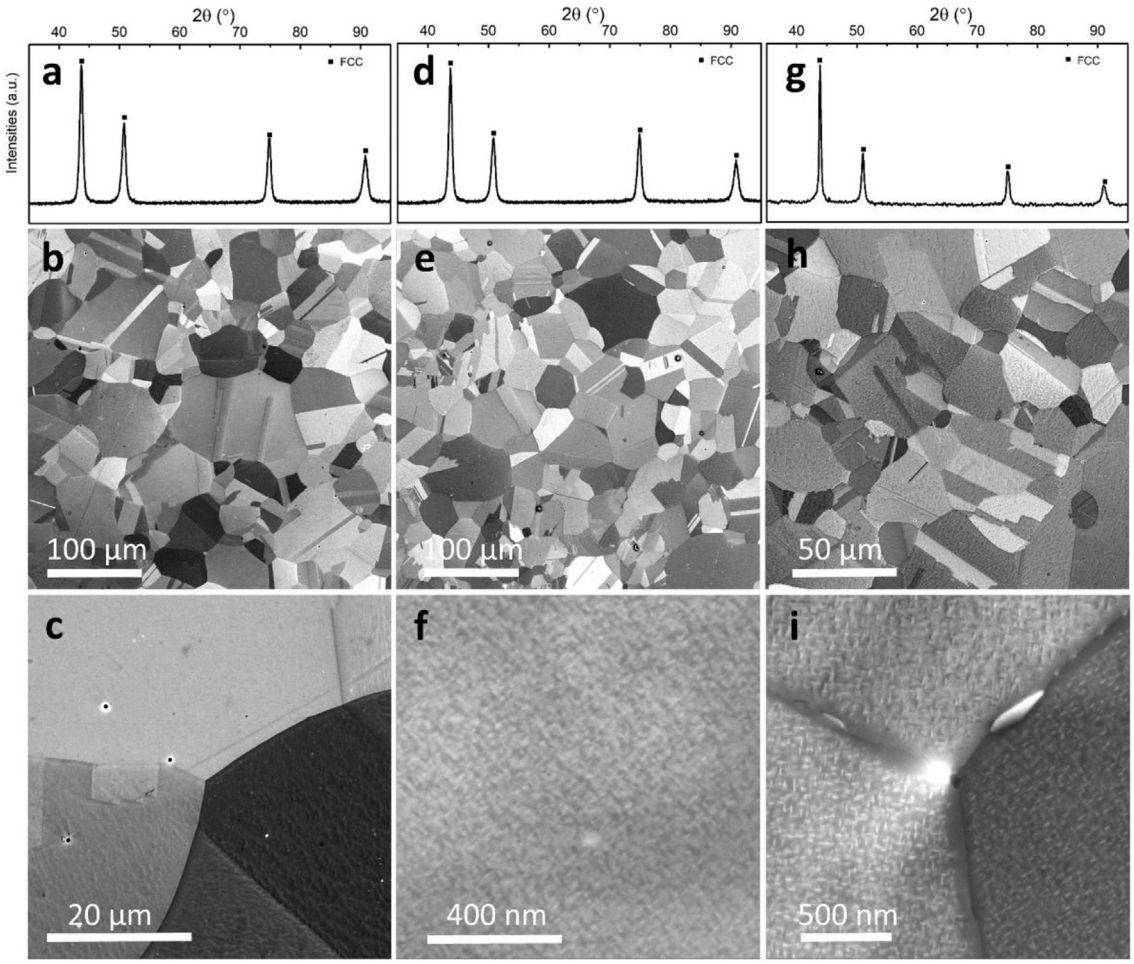

Fig. 2. (a) XRD pattern of the solid-solution $Ni_2CoCrFeNb_{0.15}$ HEA; (b–c) SEM images of the solid-solution $Ni_2CoCrFeNb_{0.15}$ HEA; (d) XRD pattern of the 80 h-annealed $Ni_2CoCrFeNb_{0.15}$ HEA; (e and f) SEM images of the 80 h-annealed $Ni_2CoCrFeNb_{0.15}$ HEA; (g) XRD pattern of the 120 h-annealed $Ni_2CoCrFeNb_{0.15}$ HEA; and (h–i) SEM images of the 120 h-annealed $Ni_2CoCrFeNb_{0.15}$ HEA.

in Fig. 2(f) shows nano-sized precipitates. The second phase precipitates homogeneously from the supersaturated solid-solution FCC matrix. The grain boundary doesn't affect its shape and size. The lattice parameters of solid-solution and annealed HEAs are very close. Although the precipitation of γ″ phase would lead to the decrease of Nb content in the matrix, the volume fraction of γ″ phase is small (~7% measured from DF TEM images) and thus the decrease of Nb content in the matrix is small and finally didn't cause obvious change in lattice parameters. The absence of diffraction peaks of the precipitates may be due to the overlap between peaks from the two phases and the small volume fraction of precipitates [28]. The grain size of the annealed HEA is similar to that of the solid-solution HEA. This is reasonable because the annealing temperature (650 °C) is equal to 0.6 T_m (Fig. 1(b)). The second possible reason is that the Nb slows down the interface mobility because of the solute-drag effect. The precipitates exhibit a slight coarsening trend when the annealing time increases to 120 h, as shown in Fig. 2(g)–(i). A small amount of third-phase occurs at grain boundaries in Fig. 2 (i), however, we are unfortunately not able to identify its crystal structure because the volume fraction of this phase is too small to be detected by TEM. It is also hard to quantify its chemical composition by using SEM-EDS since its nano-scale size. One potential method to obtain the information of the third-phase is to use CALPHAD prediction based on literature. Chaturvedi et al. [42] suggested that the γ″ phase transforms to delta phase upon aging at the grain boundary. Therefore, we suggest this phase to be a delta phase according to the CLAPHAD result (Fig. 1(c)) and its morphology (Fig. 2(i)).

4.2. TEM analysis

TEM characterization mainly focuses on the $Ni_2CoCrFeNb_{0.15}$ HEA annealed at 650 °C for 80 h. The dark field (DF) image is presented in Fig. 3(a), indicating that the precipitates have disk shapes with different crystallographic orientations. The disk-shape precipitates are ~15 nm in length and ~6 nm in width. The area fraction of the precipitates is measured to be ~7% by using DF images. Fig. 3(b) shows the representative diffraction pattern (DP) images with the zone axes of [001], [011], and [112]. The main bright dots are from the matrix and can be indexed to be a typical FCC phase. There are weak diffraction spots appearing at positions where the diffractions of disordered FCC matrix are forbidden. They collectively indicate a typical γ″ phase in the $Ni_2CoCrFeNb_{0.15}$ HEA. The crystal orientation relationship between the γ″ phase and γ matrix follows $[001]_{\gamma''}//<001>_{\gamma}$, and $\{100\}_{\gamma''}//\{100\}_{\gamma}$. A representative high resolution TEM (HRTEM) image of the γ″ phase is shown in Fig. 3(c). As can be seen, the γ″ phase lies along the $\{100\}_{\gamma}$ planes of the matrix and the size of the particles is consistent with that measured using the DF image. The lattice parameter of the γ″ phase is directly measured as $a_{\gamma''} = 3.617$ Å, $c_{\gamma''} = 7.229$ Å by using the HRTEM image.

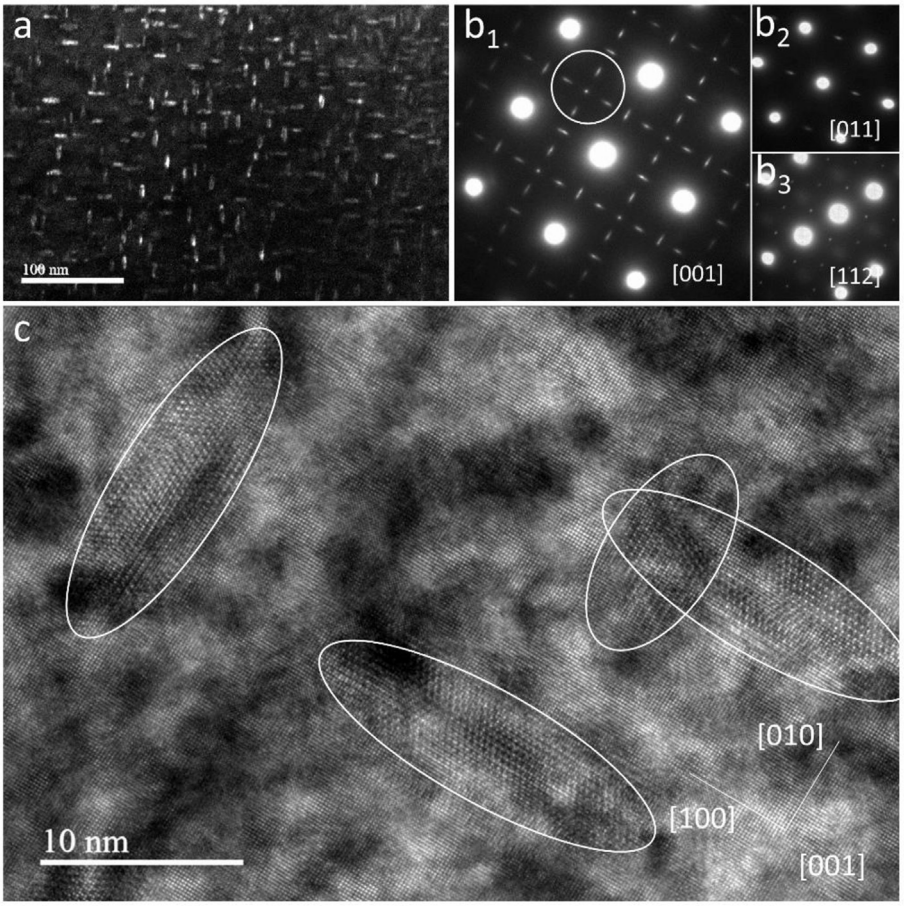

Fig. 3. (a) DF image showing the γ″ phase; (b) DP images from different zone axis; and (c) HRTEM image shows the different variants of γ″ phase.

4.3. APT characterization

The chemical compositions and the 3-demension (3D) shaped γ″ phase are analyzed by APT. The right upper box in Fig. 4(a) shows the 3D atom distribution of the 80 h − annealed $Ni_2CoCrFeNb_{0.15}$ HEA with a 50% Ni iso-concentration surface. The γ″ phase displays a disk-shape with a diameter of ~15 nm. The sliced atom maps of every single element are also presented in Fig. 4(a). The γ″ phase is enriched in Nb but depleted in Fe, Co and Cr. In order to clearly show the chemical composition partitioning between the matrix and the γ″ phase, a proximity histogram is shown in Fig. 4(b). The γ″ phase is composed of a large amount of Ni and Nb and considerable amount of Co. The quantitative chemical compositions of the γ″ phase and matrix obtained from the APT analysis are shown in Table 1.

4.4. Mechanical tests

The mechanical responses of the γ″-hardened $Ni_2CoCrFeNb_{0.15}$ HEAs are evaluated. Fig. 5(a) shows the representative engineering stress-strain curves. The solid solution treated HEA shows a yield strength of ~284 MPa, an ultimate tensile strength of ~710 MPa, and a fracture elongation of ~71%. The γ″ phase in the 80 h—annealed sample dramatically increases the yield strength to ~954 MPa and the ultimate tensile strength to ~1230 MPa. Although the precipitation strengthened HEAs exhibit a ductility decrease, its fracture elongation is still superior to the majority of intermetallic particle strengthened HEAs. Fig. 5(b) shows the strain hardening rates of both solid-solution treated and precipitation-hardened HEAs. It is clear that the strain hardening rate of the γ″-hardened HEA is much higher than that of the solid-solution HEA. According to, the strain hardening rate is proportional to the to the increase speed of $\sqrt{\rho}$ during straining. In the precipitation-hardened HEA, precipitates on the one hand pin the dislocations and promote the increase of dislocation density; and on the other hand, potentially act as dislocation emission source and again promote the dislocation density increase. Therefore, the work hardening rate of the precipitation-strengthened HEA is higher than that of the solid-solution HEA at uniform deformations stage. The fracture elongation of the precipitation strengthened $Ni_2CoCrFeNb_{0.15}$ HEAs decreases a little when the annealing time changes from 80 h to 120 h. This is due to the increase of particle size. Sundararaman et al. [43] reported that the ductility of alloys decreased sharply with the increase of particle size when the γ″ phase is larger than 10 nm. The size of γ″ phase in the current study increased from ~15 nm to ~35 nm, resulting in decrease of ductility.

Fig. 5(c–e) show the fracture surfaces of the solid-solution, 80 h-annealed, and 120 h-annealed $Ni_2CoCrFeNb_{0.15}$ HEAs. All the three HEAs shows random dimples, indicating a typical ductile fracture mechanism. The dimples of precipitation hardened HEAs display a much smaller size. The size decrease of the dimples should be due to the increase of micro-cracking probability in the γ″-strengthened HEA and the area reduction of the fracture surface. Theoretically, the dimple size depends positively on the micro-crack nucleation rate during necking and negatively on area reduction of the fracture surface. The interface between γ″ phase and matrix

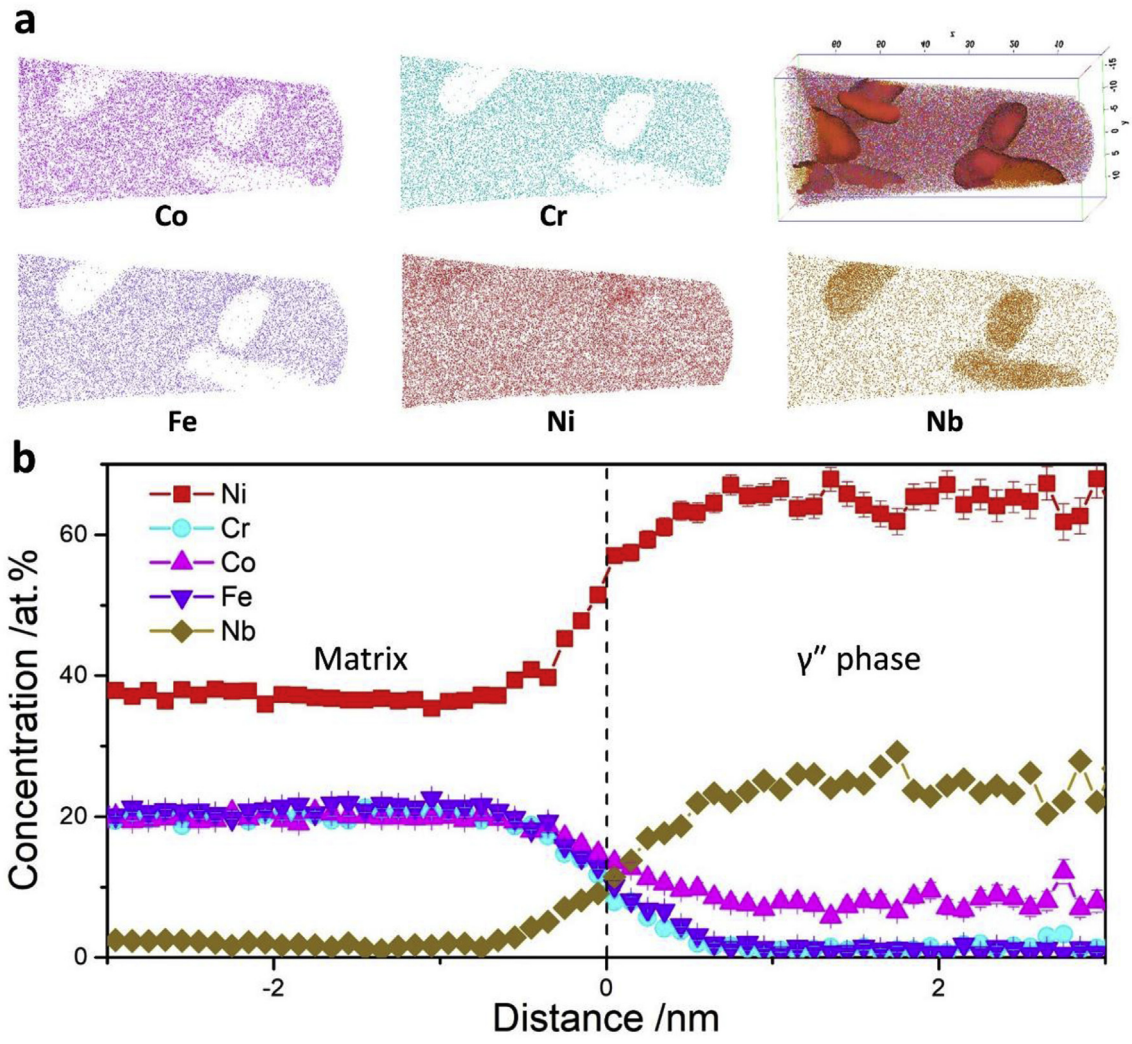

Fig. 4. (a) Atom maps of different elements and 3D construction with the 50 at.% Ni iso-concentration surface; and (b) the proximity histogram constructed across the interface between the matrix and precipitates showing the partitioning of different elements.

Table 1
Chemical compositions of matrix and γ″ phase obtained from APT (at.%).

Phases	Co	Cr	Fe	Ni	Nb
Matrix	19.5 ± 0.2	21.0 ± 0.3	21.3 ± 0.2	36.5 ± 0.2	1.5 ± 0.1
γ″	7.7 ± 0.2	1.4 ± 0.1	1.3 ± 0.1	65.2 ± 0.4	24.5 ± 0.3

enhance the crack nucleation rate and consequently decrease the crack size (dimple size when observed from fracture surface). The area reduction of the γ″-strengthened HEA (~37%) is much smaller than that of the solid-solution HEA (~77%), again resulting in a smaller dimple size.

5. Discussion

5.1. Crystallographic features of the high-entropy γ″ particles

The γ″ phase precipitating in the $Ni_2CoCrFeNb_{0.15}$ HEA shows a $D0_{22}$ superlattice (Fig. 3) which is usually based on Ni_3Nb stoichiometry [44]. The unit cell of the Ni_3Nb γ″ phase is shown in Fig. 6(a). It can be considered to be composed of two FCC unit cell placed one over another along the [001] direction. The eight corners and the center of the body centered tetragonal (BCT) unit cell are placed by Nb atoms while the rest sites are occupied by Ni atoms. Since the axial ratio of the γ″ unit cell in the present study is very close to 2, the indices of the crystal structure associated with the γ″ phase has been expressed in terms of simple FCC indices. Three γ″ variants are usually observed in a FCC matrix since the [001] axis of γ″ phase can be parallel to the <100> direction families of the FCC matrix. As shown in Fig. 6(b), the blue unit cell represents the first variant following in the crystallographic relation of $[001]_{\gamma''}//[100]_m$, and the sketch of its diffraction pattern is shown in Fig. 6(c1). Variant 2 (red unit cell in Fig. 6(b)) follows the crystal relation of $[001]_{\gamma''}//[010]_m$ and has a diffraction pattern as shown in Fig. 6(c2). The third γ″ variant, which has the crystal relation with matrix of $[001]_{\gamma''}//[001]_m$, is sketched by green unit cell in Fig. 6(b) and its diffraction pattern sketch is presented in Fig. 6(c3). The γ″ particles is too small to be characterized using TEM independently and thus the typical diffraction pattern obtained from the TEM experiment usually contains superlattice diffraction spots of all three variants, as shown in Fig. 6(c4).

In the present study, the diffraction pattern in Fig. 3(b1) shows three γ″ variants and the DF and HRTEM images (Fig. 3(a) and c) also show that the long axes of the γ″ disks have different orientations. Further analyses on the γ″ variants and their ordered

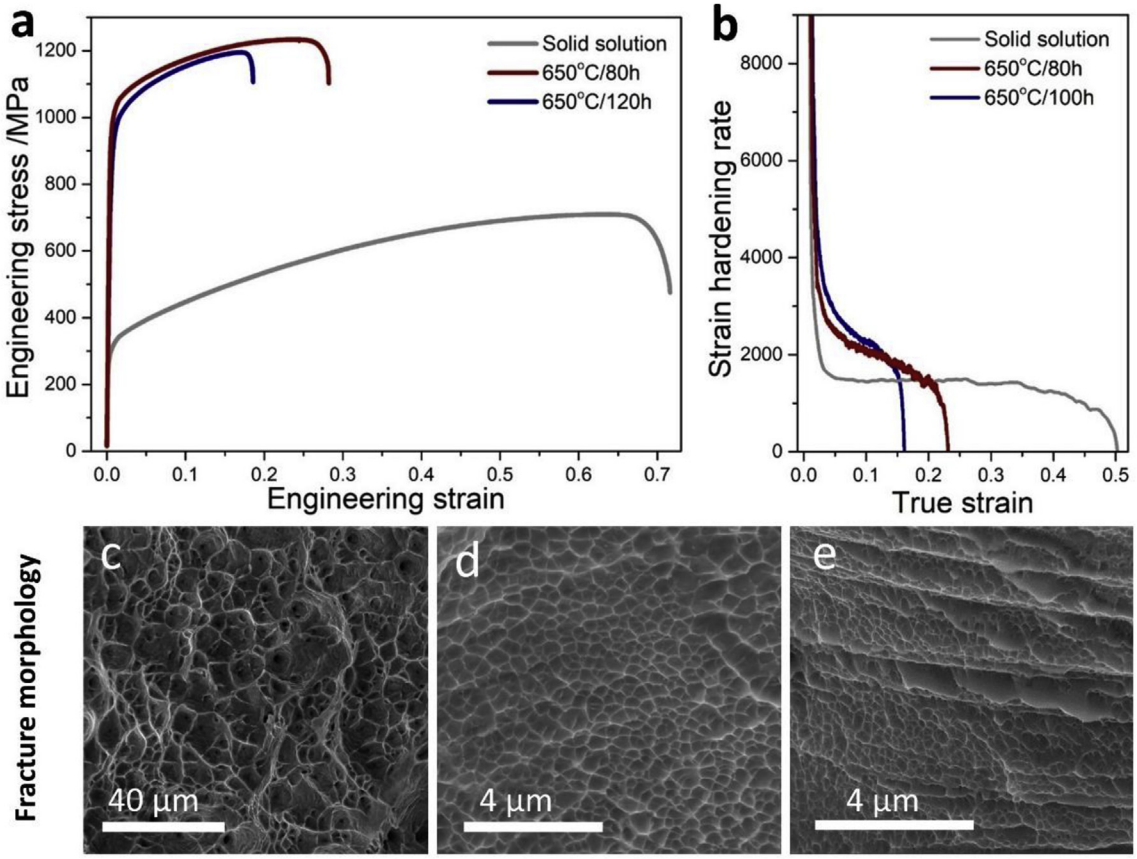

Fig. 5. (a) Representative engineering stress-strain curves of $Ni_2CoCrFeNb_{0.15}$ HEAs obtained at room temperature; (b) the strain hardening rate vs true strain plots of $Ni_2CoCrFeNb_{0.15}$ HEAs; and (c) the fracture morphologies of $Ni_2CoCrFeNb_{0.15}$ HEAs.

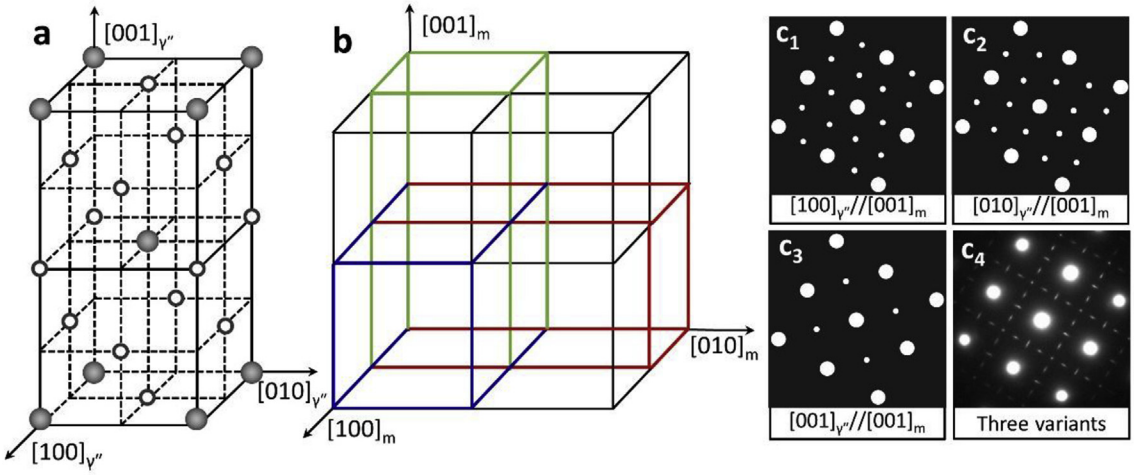

Fig. 6. (a) Sketch of $D0_{22}$ unit cell; (b) sketch of crystal relations of three γ″ variants and FCC matrix; and (c) sketch of DP image from different variants.

structures are carried out by using the fast Fourier transformation (FFT) and inverse fast Fourier transformation (IFFT). Fig. 7(a) shows the IFFT image of a single γ″ variant and its FFT image is shown in Fig. 7(b). A crystallographic relation of $[100]_{\gamma''}//[001]_m$ is obtained from the FFT image. According to the IFFT image, we can see that the matrix lattice shows a same contrast while the γ″ lattice shows the contrast variation, which is caused by the ordered structure of the γ″ phase. The inset sketch in Fig. 7(a) shows the contrast change in the γ″ lattice. The yellow ball represents the brighter spots and the blue ball represents the darker spots. As can be seen, the yellow ball layer occurs repeatedly every four {420} crystal planes, resulting in the superlattice diffraction spots at position of $(1\frac{1}{2}0)$ and (210) planes (Fig. 7(b)). This is consistent with the ordering of Nb atom in Fig. 6(a), indicating that the corners and center of the present high-entropy γ″ is also occupied mainly by Nb. Fig. 7(c and d) show the second γ″ variant observed in the HRTEM image. This γ″ variant shows the same lattice ordering but follows a different crystal relation of $[010]_{\gamma''}//[001]_m$. The third γ″ variant that obeys

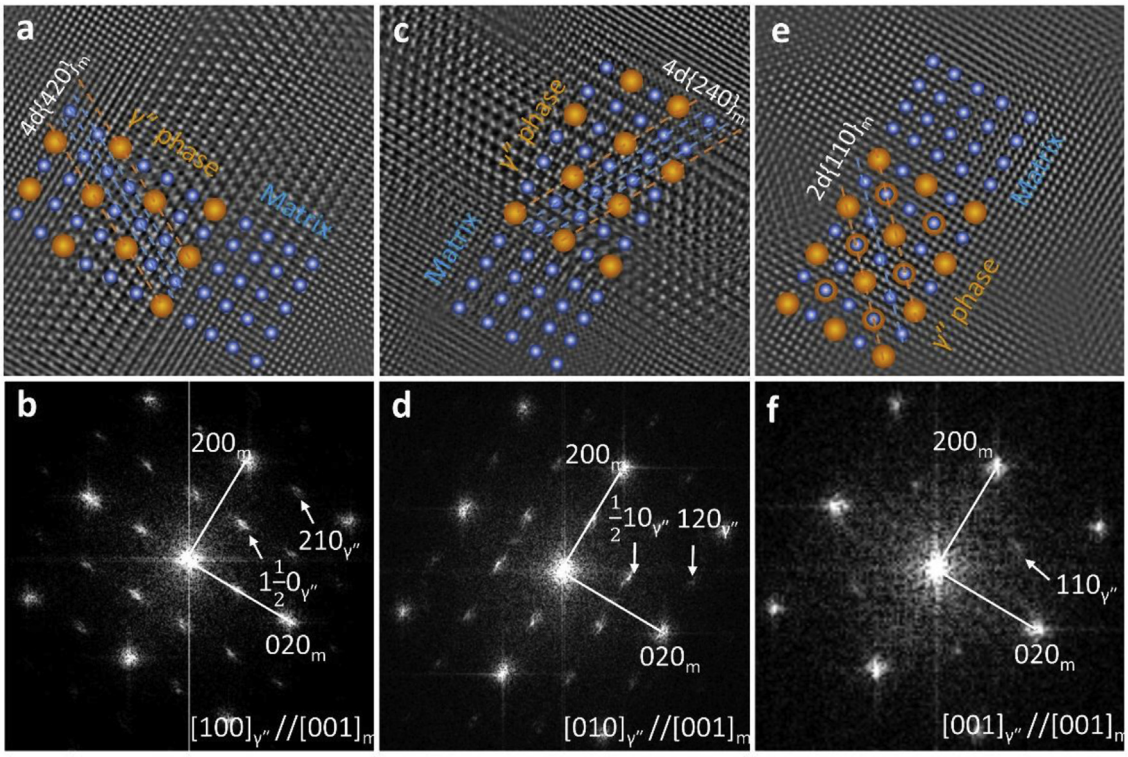

Fig. 7. (a) IFFT images and sketch insets showing the ordering of variant 1; (b) corresponding FFT of (a); (c) IFFT images and sketch insets showing the ordering of variant 2; (d) corresponding FFT of (c); (e) IFFT images and sketch insets showing the ordering of variant 3; and (f) corresponding FFT of (e).

$[001]_{\gamma''}//[001]_m$ is presented in Fig. 7(e and f). From the $[001]_{\gamma''}$ direction the brighter spots are found to occur repeatedly every two (110) crystal planes (Fig. 7(e)), leading to the formation of superlattice diffraction of $(110)_{\gamma''}$ plane (Fig. 7(f)).

The γ″ phase in the present HEA shows $D0_{22}$ superlattice and thus has three variants in the FCC high entropy matrix. However, the chemical composition of γ″ phase in the present HEA is far from the Ni_3Nb stoichiometry. The γ″ phase in the present study consists of not only Ni and Nb but also as much as ~10% of Co, Fe and Cr in total (Table 1) while in literature only very small amount of Fe and Cr has been reported in the γ″ phase [45]. The Nb content obtained from APT is 24.5% (Table 1), indicating that apart from Nb there must be other atoms occupying the corners and center of the BCT unit cell. In the previous studies, Chaturvedi et al. [42] demonstrated that the addition of a small amount of Fe facilitates the γ″ formation in a $Ni_{36}Co_{37}Cr_{16}Fe_3Nb_8$ alloy. Kusabiraki et al. [45] reported that the Fe tends to substitute the Nb site of the γ″ phase in a $Ni_{69}Cr_{15}Fe_8Nb_6$ alloy. Sugimura et al. [46] theoretically proved that the Co and Cr prefer to substitute Ni in a Ni_3Nb δ phase, which is the stable form of γ″ phase in superalloys, while the Fe can substitute either Ni or Nb. In the current work, the Fe content of γ″ phase is ~1.3% (Table 1) and thus the Fe atoms occupy both the Ni and Nb sites and the Co and Cr take the Ni sites in the present γ″ phase. Therefore, a $(Ni,Co,Cr,Fe)_3(Nb,Fe)$ stoichiometry for the present γ″ phase could be suggested. Note that the current TEM and APT are not able to differentiate the Ni, Co, Fe and Cr atoms efficiently in a crystal unit cell and experimental data in literature is also limited, so this statement is somewhat rough where more insightful study is required.

5.2. Strengthening mechanisms

Strengthening mechanisms for polycrystalline materials are summarized as solid solution hardening (σ_s), dislocation strengthening (σ_d), grain boundary hardening (σ_g), precipitation hardening (σ_p). The yield strength can be expressed as a simple summation of every individual contribution. In the current study, all samples are fully recrystallized before aging at low temperature. Therefore, the dislocation strengthening can be ignored and the yield strength can be calculated by

$$\sigma_{0.2} = \sigma_0 + \Delta\sigma_s + \Delta\sigma_g + \Delta\sigma_p \quad (1)$$

where σ_0 means the intrinsic strength.

As for the γ″-hardened $Ni_2CoCrFeNb_{0.15}$ HEA, the Nb has much larger atom radius than those of other four elements, so the addition of Nb into the $Ni_2CoCrFe$ matrix will cause solid solution strengthening. The traditional solid solution strengthening mechanism is based on the dilute solution alloys, where strengthening effect is due to the strain field arising from mismatch between solute and solvent [47]. However, it is challenging to evaluate the strengthening effect by applying traditional solid solution strengthening mechanism to HEAs because the solvent and solute are not distinguishable for HEAs due to their equal or near-equal chemical compositions. To evaluate the solid solution strengthening effect in the present study, a recrystallized single-phase $Ni_2CoCrFe$ HEA is prepared and tested. The yield strength of the $Ni_2CoCrFe$ HEA is measured to be 197 MPa (not shown in the figures). It should be noted that the grain size of the single-phase $Ni_2CoCrFe$ HEA (~103 μm) is larger than that of the solid-solution $Ni_2CoCrFeNb_{0.15}$ HEA (~45 μm). The effect of grain size on the yield strength can be well described by Hall-Petch relation, $\sigma_g = \sigma_0 + k_y \frac{1}{d^{1/2}}$, where k_y is the strengthening coefficient. The strength increase caused by refining grain size can be derived: $\Delta\sigma_g = k_y(d_2^{-1/2} - d_1^{-1/2})$. In this study, we adopt the k_y value (840 MPa $\mu m^{1/2}$) calculated from the tensile tests of CoCrFeNi HEA

at room temperature [48] and obtain the $\Delta\sigma_g = 45.3$ MPa. Therefore, the increase of yield strength caused by solid solution hardening can be calculated to be $\Delta\sigma_s = 284-197-45.3 = 41.7$ MPa. According to equation (1), the strength increases from precipitation strengthening is calculated to be $\Delta\sigma_p = 954-284 = 670$ MPa.

Fig. 8(a) and its inset table summarize the strength contributions of the different strengthening mechanisms to the γ″-hardened $Ni_2CoCrFeNb_{0.15}$ HEA. It is clear that the precipitation strengthening is the main reason for its high yield strength. Fig. 8(b) shows the comparative results of the strength increase and elongation retention rate (elongation retention $= \varepsilon_p/\varepsilon_{ss}$, where ε_p is the elongation of precipitate-hardened HEAs and ε_{ss} is the elongation of solid-solution HEAs) caused by different precipitates in literature. The intermetallic compounds forming during solidification effectively strengthen the alloys but cause severe embrittlement (the left lower part in Fig. 8(b)). Uniformly distributed intermetallic particles show a better strengthening effect as reported by Liu et al. [32] and Ming et al. [33] due to the high work hardening exponent of the high entropy matrix. The γ′-strengthened HEAs are shown in the red area. Comparing with intermetallic-strengthened HEAs, γ′-strengthened HEAs show a higher ductility because the γ′ phase is fully coherent with the FCC matrix [29]. The star in Fig. 8(b) represents the γ″-hardened $Ni_2CoCrFeNb_{0.15}$ HEA in the current work, and it shows the best combined effects on the strength increase and elongation retention. As a result, the γ″-hardened $Ni_2CoCrFeNb_{0.15}$ HEA shows a superior strength-ductility combination. Fig. 8(c) compares the yield strength and ductility of these reported precipitation strengthened HEAs together with the HEA developed in the present study. In terms of the strength-ductility trade-off, it appears that the γ″ precipitate is more efficient in precipitation strengthening than γ′ and other incoherent intermetallic particles when they are in the same volume fractions and particle sizes.

5.3. Reasons for superior strengthening effect of $D0_{22}$ superlatices

The precipitation strengthening has been summarized through different interaction mechanisms [35]. Those for which theories have been developed when a dislocation cuts through particles include: 1) chemical strengthening, 2) stacking-fault strengthening, 3) modulus strengthening, 4) coherency strengthening, and 5) ordering strengthening. The first three mechanisms are usually ignored since they contribute much less to the yield strength when compared to coherency strengthening and ordering strengthening. The dislocation can also interact with particles through Orowan mechanism when the particles are not easy to cut though. In order to show the advantage of the γ″ phase in precipitation strengthening, we will compare the strengthening effects of γ″, γ′, and intermetallic particles with same size and volume fractions.

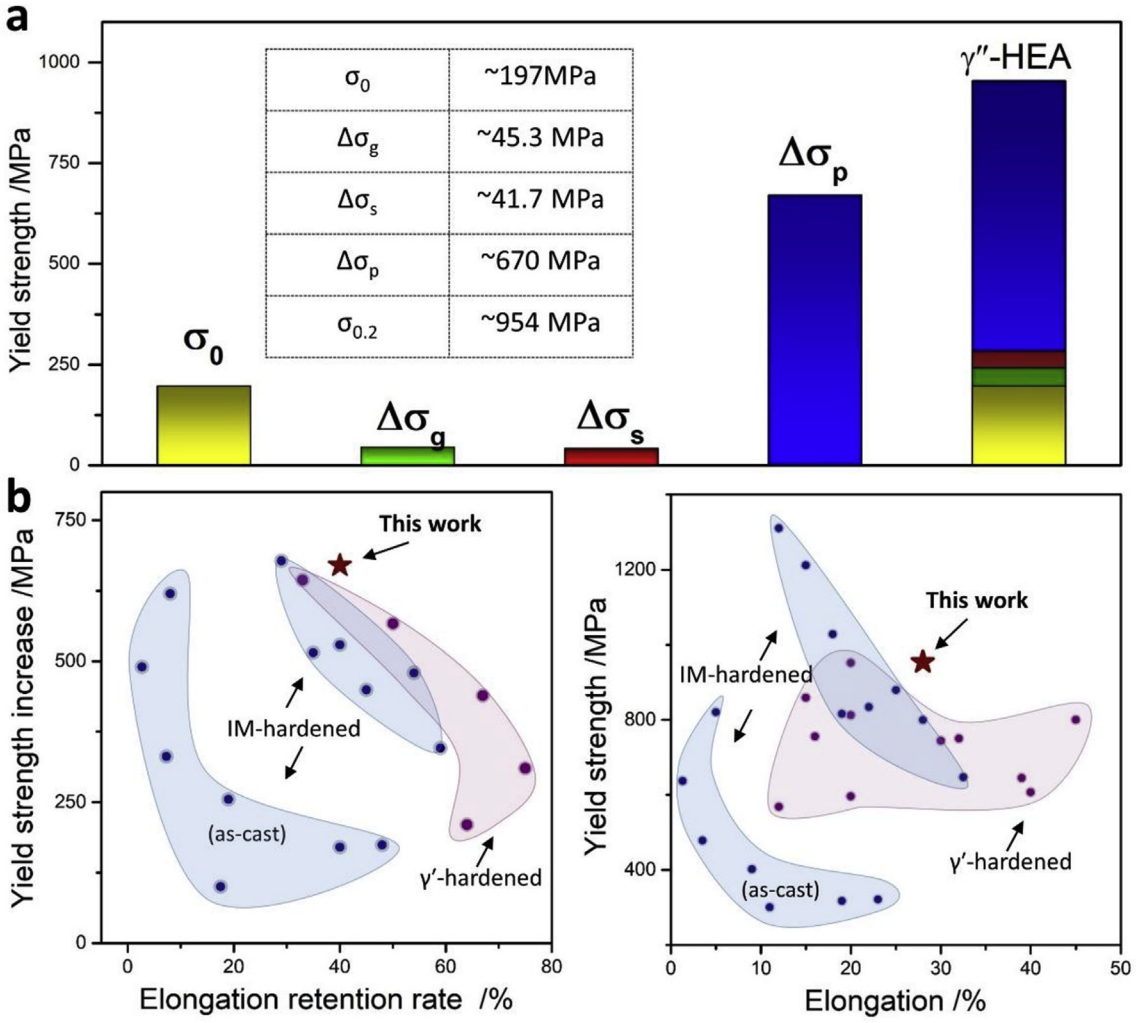

Fig. 8. (a) Contributions of different strengthening mechanisms; (b) the comparative results of yield strength increase and ductility retention; (c) Ashby plot showing the advantage of γ″ strengthened HEAs. Mechanical properties obtained from $CoCrFeNiMnAl_x$ [15], $CoCrFeNiAl_{0.5}$ [51], $(CoCrFeNi)_{94}Ti_2Al_4$ [27], $(CoCrNi)_{94}Ti_3Al_3$ [28], $Al_{0.2}Co_{1.5}CrFeNi_{1.5}Ti_{0.3}$ [29], $Al_{3.31}Co_{27}Cr_{18}Fe_{18}Ni_{27.27}Ti_{5.78}$ [52], $(FeNi)_{67}Cr_{15}Mn_{10}Al_{8-x}Ti_x$ [41], $Al_{10}Co_{25}Cr_8Fe_{15}Ni_{36}Ti_6$ [53], $CoCrFeNiMo_{0.3}$ [32], $Cr_{15}Fe_{20}Co_{35}Ni_{20}Mo_{10}$ [33].

For the γ″ phase, numerous previous works demonstrated that the coherency strengthening and ordering strengthening jointly dominate the yield strength. Oblak et al. [49], have derived the equation of coherency strengthening and ordering strengthening for γ″ phase,

$$\Delta\sigma_{coherency} = 1.7MG|\varepsilon|^{3/2}\left[\frac{h^2 f(1-\beta)}{2bR}\right]^{1/2} \quad (2)$$

$$\Delta\sigma^{\gamma''}_{ordering} = M\left(\frac{\gamma_{APB}}{2b}\right)\left\{\left[\frac{4\gamma_{APB}f}{\pi T}\left(\frac{\sqrt{6}Rh}{3}\right)^{1/2}\right]^{1/2} - \beta f\right\} \quad (3)$$

Where G is the shear modulus, b is the magnitude of Burger's vector, f is the volume fraction of precipitates, ε is the tetragonal lattice misfit, R is the real diameter of the particles, h is the half thickness of the particles, M is Taylor factor (3.06 for an fcc polycrystalline matrix),β is a constant and equal to 1/3 when all three variants are observed, the γ_{APB} is the antiphase boundary energy of the γ″ phase, and T is the line tension which is taken to be *0.5* Gb^2. The ordering strengthening is considered when a pairwise of a/2<110> dislocations cut through the γ″ phase since this type of deformation mode is observed in γ″-strengthened superalloys [43].

In the present study, the tetragonal lattice misfit between γ″ phase and matrix is measured to be 0.012 from HRTEM images. The volume fraction of γ″ phase is measured to be 0.07 from DF image. R and h are taken to be 15 and 5 nm according to the DF images. Stress calculations were carried out using the values $\gamma_{APB} = 0.296$ J/m^2, G = 77 GPa, following Oblak et al. [49]. The calculated stress increases were shown in Table 2. It can be seen that the sum of ordering strengthening (480 MPa) and coherency strengthening (207 MPa) of γ″ phase is remarkably consistent with the experimental yield strength increase (670 MPa) in the present study.

As for the γ′-strengthened HEAs, recent literature showed that the ordering strengthening is the main contribution when the particle size is smaller than ~35 nm [28,29]. The strength increase caused by ordering strengthening of γ′ phase is given by Ref. [35].

$$\Delta\sigma^{\gamma'}_{ordering} = 0.81M\frac{\gamma_{APB}}{2b}\left(\frac{3\pi f}{8}\right)^{1/2} \quad (4)$$

antiphase boundary energy of the γ′ phase is usually less than 0.2 J/m^2 and we adopted 0.12 J/m^2 here, following He et al. [27]. Consider that the volume fraction and particle size of γ′ phase are also 7% and 15 nm, the ordering strengthening contribution can be calculated to be 169 MPa, as shown in Table 2.

Finally, we assume that there were intermetallic particles with particle size of 15 nm and volume fraction of 7%, instead of γ″ phase or γ′ phase, in the FCC matrix, where the Orowan mechanism usually dominates. The yield strength increase caused by Orowan mechanism can be predicted by Ashby-Orowan relation [50],

$$\Delta\sigma_{orowan} = 0.538\frac{Gbf^{1/2}}{r}\ln\left(\frac{r}{2b}\right) \quad (5)$$

As shown in Table 2, the intermetallic particles can cause good stress increase (625 MPa) but the Orowan looping mechanism usually leads to the severe ductility decrease [29,43]. In Fig. 8(c), the ductility of intermetallic particles strengthened HEAs is much lower than that of the γ″ phase strengthened HEA when the strength is comparable. In contrast, the γ′ phase causes only 169 MPa stress increase when the volume fraction and particle size are same with the γ″ phase. Comparing equations (3) and (4), we can draw two obvious reasons for the remarkable advantages of γ″ phase: (a) the antiphase boundary energy of γ″ phase is much higher than that of the γ′ phase; (b) the tetragonal lattice misfit (usually 0.01–0.03) between γ″ phase and matrix is much higher than that (usually ranges 0.0035 to 0.001) of the γ′ phase and consequently causes higher coherency strengthening [35]. Therefore, the γ″ phase strengthened HEAs showed better strength when compared with γ′-phase strengthened HEAs and better ductility when compared with intermetallic particle strengthened HEAs (Fig. 8(b-c)).

Table 2
Calculated stress increase caused by different precipitates (volume fraction of 7%).

Precipitates	$\Delta\sigma_{ordering}$ (MPa)	$\Delta\sigma_{coherency}$ (MPa)	$\Delta\sigma_{orowan}$ (MPa)
γ″	480	207	–
γ′	169	–	–
Intermetallics	–	–	625

6. Conclusion

The present study proposed a novel OVEC principle for the design of γ″ phase with $D0_{22}$ superlattice crystal structure in HEAs. Following in this principle, we developed a γ″ phase strengthened HEA with a minor addition of Nb. The γ″ phase showed superior strengthening effect and resulted in excellent yield strength-ductility combination. The characteristics of the newly designed γ″ phase have been investigated using SEM, TEM, APT and the strengthening mechanisms have been discussed. The following conclusions can be drawn.

- An OVEC design strategy was proposed to design γ″ phase in HEAs. The γ″ phase tends to form when the OVEC value of HEAs is higher than 8.4. Besides, the elements from Group VB have been found to facilitate the precipitation of the γ″ phase in FCC HEAs;
- A γ″ phase strengthened $Ni_2CoCrFeNb_{0.15}$ HEA was developed. The γ″ phase precipitated homogenously from the matrix. APT analysis showed the γ″ phase is different from Ni_3Nb-type γ″ phase in superallys and has a chemical stoichiometry of (Ni,Co,Cr,Fe)$_3$(Nb,Fe). A careful TEM inspection showed that the γ″ phase has a typical $D0_{22}$ superlattice crystal structure. The crystallographic relation between the γ″ phase and matrix follows $[001]_{\gamma''}//<001>_{\gamma}$, and $\{100\}_{\gamma''}//\{100\}_{\gamma}$ and consequently three different variants of γ″ phase have been observed.
- The γ″ phase showed superior strengthening effect. The γ″ precipitates with a volume fraction of 7% enhanced the yield strength of the $Ni_2CoCrFeNb_{0.15}$ HEA by 670 MPa, resulting in excellent combination of yield strength (954 MPa) and ductility (27%);
- The strengthening mechanisms of the γ″ phase are mainly attributed to ordering strengthening and coherency strengthening.

In summary, a convenient design strategy for γ″ phase in FCC HEAs has been proposed and proved to be effective. The γ″ phase strengthened HEA showed excellent yield strength and ductility. Our investigations accelerate the development of design of precipitation strengthened HEAs and provide a new and good candidate for structural HEAs.

Acknowledgment

The work was financially supported by National Natural Science foundation of China (ZJW, Grant No. 51471133 and 51771149), the Hong Kong Research Grant Council (RGC) (JJK, Hong Kong Grant No.

CityU 11212915), the Excellent Doctorate Foundation of Northwestern Polytechnical University (FH, Grant No. CX201805)

Appendix

Table. S1
The OVEC value and type of precipitates of different CCAs.

Alloys	Temperatures	Precipitates	VEC	References
Ni75V25	quench	γ″	8.75	[54]#
Ni72V25Fe3	quench	γ″	8.69	[54]#
Ni75V23Nb2	quench	γ″	8.75	[54]#
Ni68V25Co7	quench	γ″	8.68	[54]#
Ni75V15Fe8Nb2	800oC	γ″	8.99	[54]#
Ni82V18	800°C	γ″	9.1	[54]#
Co37Ni36Cr16Fe3Nb8	700oC	γ″	8.708	[42]*
Co35Ni35Cr15Fe3Nb12	700°C	γ″	8.495	[42]*
Co34Ni33Cr15Fe6Nb12	700°C	γ″	8.443	[42]*
Ni31.8Fe65.2Ta3	550 − 750°C	γ″	8.546	[55]#
Co8.2Ni29Fe59.8Ta3	550 − 750°C	γ″	8.572	[55]#
Co12.4Ni29Fe55.6Ta3	550 − 750°C	γ″	8.614	[55]#
Ni63Co27Ta10	685°C	γ″	9.23	[56]#
Ni62.1Co27.9Ta10	685°C	γ″	9.221	[56]#
Ni61.1Co28.9Ta10	685°C	γ″	9.211	[56]#
Ni69Cr15Fe8Nb6	670 − 800°C	γ″	8.74	[45]#
Ni84.5Nb12.5Fe3	500°C	γ″	9.315	[57]#
Ni61Cr20W18Mo1	600 − 700°C	γ″	8.713	[58]*
Ni60.15Cr14.7Fe24.8Nb4.85	650°C − 800°C	γ″	8.736	[59]*
Ni66Cr26W6Ti2	700°C	γ″	8.6	[60]#
Ni58Co37Nb5	500°C	γ″	9.38	[61]#
(CoCrNi)94Ti3Al3	800°C	γ′	8.045	[28]#
Al0.2Co1.5CrFeNi1.5Ti0.3	800°C	γ′	8.063	[29]#
Al3.31Co27Cr18Fe18Ni27.27Ti5.78	750°C	γ′	8.0075	[52]#
Al10Co25Cr8Fe15Ni36Ti6	900°C	γ′	8.07	[53]#
(CoCrFeNi)94Ti2Al4	650°C	γ′	7.955	[27]#
Ni2CoCrFeAl0.1Ti0.2	800°C	γ′	8.256	Unpublished
Ni2CoCrFeAl0.15Ti0.15	800°C	γ′	8.243	Unpublished
Ni2CoCrFeAl0.2Ti0.1	800°C	γ′	8.216	Unpublished
Ni2CoCrFeNb0.15	650°C	γ″	8.495	Present
NiCoCrFeNb0.25	750°C	ε	8.06	[40]#

* means in weight percent and # means in atom percent.

References

[1] J.W. Yeh, S.K. Chen, S.J. Lin, J.Y. Gan, T.S. Chin, T.T. Shun, C.H. Tsau, S.Y. Chang, Nanostructured high-entropy alloys with multiple principal elements: novel alloy design concepts and outcomes, Adv. Eng. Mater. 6 (5) (2004) 299–303.

[2] D.B. Miracle, O.N. Senkov, A critical review of high entropy alloys and related concepts, Acta Mater. 122 (2017) 448–511.

[3] B. Cantor, I.T.H. Chang, P. Knight, A.J.B. Vincent, Microstructural development in equiatomic multicomponent alloys, Mater. Sci. Eng., A 375–377 (2004) 213–218.

[4] O. Senkov, G. Wilks, J. Scott, D. Miracle, Mechanical properties of Nb25Mo25Ta25W25 and V20Nb20Mo20Ta20W20 refractory high entropy alloys, Intermetallics 19 (5) (2011) 698–706.

[5] M. Feuerbacher, M. Heidelmann, C. Thomas, Hexagonal high-entropy alloys, Mater. Res. Lett. 3 (1) (2015) 1–6.

[6] B. Gludovatz, A. Hohenwarter, D. Catoor, E.H. Chang, E.P. George, R.O. Ritchie, A fracture-resistant high-entropy alloy for cryogenic applications, Science 345 (6201) (2014) 1153–1158.

[7] Y.H. Jo, S. Jung, W.M. Choi, S.S. Sohn, H.S. Kim, B.J. Lee, N.J. Kim, S. Lee, Cryogenic strength improvement by utilizing room-temperature deformation twinning in a partially recrystallized VCrMnFeCoNi high-entropy alloy, Nat. Commun. 8 (2017) 15719.

[8] Z. Zhang, M.M. Mao, J. Wang, B. Gludovatz, Z. Zhang, S.X. Mao, E.P. George, Q. Yu, R.O. Ritchie, Nanoscale origins of the damage tolerance of the high-entropy alloy CrMnFeCoNi, Nat. Commun. 6 (2015) 10143.

[9] F. Otto, A. Dlouhý, C. Somsen, H. Bei, G. Eggeler, E.P. George, The influences of temperature and microstructure on the tensile properties of a CoCrFeMnNi high-entropy alloy, Acta Mater. 61 (15) (2013) 5743–5755.

[10] J. Miao, C.E. Slone, T.M. Smith, C. Niu, H. Bei, M. Ghazisaeidi, G.M. Pharr, M.J. Mills, The evolution of the deformation substructure in a Ni-Co-Cr equiatomic solid solution alloy, Acta Mater. 132 (2017) 35–48.

[11] F. Granberg, K. Nordlund, M.W. Ullah, K. Jin, C. Lu, H. Bei, L. Wang, F. Djurabekova, W. Weber, Y. Zhang, Mechanism of radiation damage reduction in equiatomic multicomponent single phase alloys, Phys. Rev. Lett. 116 (13) (2016) 135504.

[12] Y.Y. Chen, T. Duval, U.D. Hung, J.W. Yeh, H.C. Shih, Microstructure and electrochemical properties of high entropy alloys—a comparison with type-304 stainless steel, Corros. Sci. 47 (9) (2005) 2257–2279.

[13] Z. Fu, W. Chen, H. Wen, D. Zhang, Z. Chen, B. Zheng, Y. Zhou, E.J. Lavernia, Microstructure and strengthening mechanisms in an FCC structured single-phase nanocrystalline Co25Ni25Fe25Al7.5Cu17.5 high-entropy alloy, Acta Mater. 107 (2016) 59–71.

[14] B. Geddes, Superalloys: Alloying and Performance, Asm International, 2010.

[15] J.Y. He, W.H. Liu, H. Wang, Y. Wu, X.J. Liu, T.G. Nieh, Z.P. Lu, Effects of Al addition on structural evolution and tensile properties of the FeCoNiCrMn high-entropy alloy system, Acta Mater. 62 (0) (2014) 105–113.

[16] F. He, Z. Wang, M. Zhu, J. Li, Y. Dang, J. Wang, The phase stability of Ni2CrFeMox multi-principal-component alloys with medium configurational entropy, Mater. Des. 85 (0) (2015) 1–6.

[17] L. Jiang, Y. Lu, Y. Dong, T. Wang, Z. Cao, T. Li, Annealing effects on the microstructure and properties of bulk high-entropy CoCrFeNiTi 0.5 alloy casting ingot, Intermetallics 44 (2014) 37–43.

[18] N. Park, I. Watanabe, D. Terada, Y. Yokoyama, P. Liaw, N. Tsuji, Recrystallization behavior of CoCrCuFeNi high-entropy alloy, Metall. Mater. Trans. 46 (4) (2015) 1481–1487.

[19] W.H. Liu, Y. Wu, J.Y. He, T.G. Nieh, Z.P. Lu, Grain growth and the Hall–Petch relationship in a high-entropy FeCrNiCoMn alloy, Scripta Mater. 68 (7) (2013) 526–529.

[20] Z. Fu, B.E. MacDonald, D. Zhang, B. Wu, W. Chen, J. Ivanisenko, H. Hahn, E.J. Lavernia, Fcc nanostructured TiFeCoNi alloy with multi-scale grains and enhanced plasticity, Scripta Mater. 143 (2018) 108–112.

[21] Z. Li, K.G. Pradeep, Y. Deng, D. Raabe, C.C. Tasan, Metastable high-entropy dual-phase alloys overcome the strength-ductility trade-off, Nature 534 (7606) (2016) 227–230.

[22] Y. Deng, C.C. Tasan, K.G. Pradeep, H. Springer, A. Kostka, D. Raabe, Design of a twinning-induced plasticity high entropy alloy, Acta Mater. 94 (0) (2015) 124–133.

[23] F. He, Z. Wang, Q. Wu, D. Chen, T. Yang, J. Li, J. Wang, C.T. Liu, J.-j. Kai, Tuning the defects in face centered cubic high entropy alloy via temperature-dependent stacking fault energy, Scripta Mater. 155 (2018) 134–138.
[24] S. Wei, F. He, C.C. Tasan, Metastability in high-entropy alloys: a review, J. Mater. Res. 33 (19) (2018) 2924–2937.
[25] F. He, Z. Wang, S. Niu, Q. Wu, J. Li, J. Wang, C.T. Liu, Y. Dang, Strengthening the CoCrFeNiNb0.25 high entropy alloy by FCC precipitate, J. Alloy. Comp. 667 (2016) 53–57.
[26] T. Yang, Y. Zhao, W. Liu, J. Kai, C. Liu, L12-strengthened high-entropy alloys for advanced structural applications, J. Mater. Res. (2018) 1–15.
[27] J.Y. He, H. Wang, H.L. Huang, X.D. Xu, M.W. Chen, Y. Wu, X.J. Liu, T.G. Nieh, K. An, Z.P. Lu, A precipitation-hardened high-entropy alloy with outstanding tensile properties, Acta Mater. 102 (2016) 187–196.
[28] Y.L. Zhao, T. Yang, Y. Tong, J. Wang, J.H. Luan, Z.B. Jiao, D. Chen, Y. Yang, A. Hu, C.T. Liu, J.J. Kai, Heterogeneous precipitation behavior and stacking-fault-mediated deformation in a CoCrNi-based medium-entropy alloy, Acta Mater. 138 (2017) 72–82.
[29] K. Ming, X. Bi, J. Wang, Realizing strength-ductility combination of coarse-grained Al0.2Co1.5CrFeNi1.5Ti0.3 alloy via nano-sized, coherent precipitates, Int. J. Plast. 100 (2018) 177–191.
[30] L. Zhang, Y. Zhou, X. Jin, X. Du, B. Li, Precipitation-hardened high entropy alloys with excellent tensile properties, Mater. Sci. Eng., A 732 (2018) 186–191.
[31] T. Yang, Y.L. Zhao, Y. Tong, Z.B. Jiao, J. Wei, J.X. Cai, X.D. Han, D. Chen, A. Hu, J.J. Kai, K. Lu, Y. Liu, C.T. Liu, Multicomponent intermetallic nanoparticles and superb mechanical behaviors of complex alloys, Science 362 (6417) (2018) 933–937.
[32] W.H. Liu, Z.P. Lu, J.Y. He, J.H. Luan, Z.J. Wang, B. Liu, Y. Liu, M.W. Chen, C.T. Liu, Ductile CoCrFeNiMox high entropy alloys strengthened by hard intermetallic phases, Acta Mater. 116 (2016) 332–342.
[33] K. Ming, X. Bi, J. Wang, Precipitation strengthening of ductile Cr15Fe20-Co35Ni20Mo10 alloys, Scripta Mater. 137 (2017) 88–93.
[34] M.C. Chaturvedi, D.W. Chung, Yielding behavior of a γy-precipitation strengthened Co Ni Cr Nb Fe alloy, Metall. Trans. A 12 (1) (1981) 77–81.
[35] A.J. Ardell, Precipitation hardening, Metall. Trans. A 16 (12) (1985) 2131–2165.
[36] B. Han, J. Wei, F. He, D. Chen, Z. Wang, A. Hu, W. Zhou, J. Kai, Elemental phase partitioning in the γ-γ″ Ni2CoFeCrNb0.15 high entropy alloy, Entropy 20 (12) (2018) 910.
[37] C.T. Liu, J.O. Stiegler, Ductile ordered intermetallic alloys, Science 226 (4675) (1984) 636–642.
[38] S. Guo, C. Ng, J. Lu, C.T. Liu, Effect of valence electron concentration on stability of fcc or bcc phase in high entropy alloys, J. Appl. Phys. 109 (10) (2011).
[39] T. Yang, Y.L. Zhao, W.H. Liu, J.H. Zhu, J.J. Kai, C.T. Liu, Ductilizing brittle high-entropy alloys via tailoring valence electron concentrations of precipitates by controlled elemental partitioning, Materials Research Letters 6 (10) (2018) 600–606.
[40] F. He, Z. Wang, J. Wang, Q. Wu, D. Chen, B. Han, J. Li, J. Wang, J.J. Kai, Abnormal γ″ - ε phase transformation in the CoCrFeNiNb0.25 high entropy alloy, Scripta Mater. 146 (2018) 281–285.
[41] Y.L. Zhao, T. Yang, J.H. Zhu, D. Chen, Y. Yang, A. Hu, C.T. Liu, J.J. Kai, Development of high-strength Co-free high-entropy alloys hardened by nanosized precipitates, Scripta Mater. 148 (2018) 51–55.
[42] M.C. Chaturvedi, D.W. Chung, Effect of iron addition on the precipitation behavior of CoNiCr alloys containing Nb, Metall. Trans. A 10 (11) (1979) 1579–1585.
[43] M. Sundararaman, P. Mukhopadhyay, S. Banerjee, Deformation behaviour of γ″ strengthened inconel 718, Acta Metall. 36 (4) (1988) 847–864.
[44] M. Sundararaman, P. Mukhopadhyay, S. Banerjee, Some aspects of the precipitation of metastable intermetallic phases in INCONEL 718, Metall. Trans. A 23 (7) (1992) 2015–2028.
[45] K. Kusabiraki, H. Komatsu, S. Ikeuchi, Lattice constants and compositions of the metastable Ni3Nb phase precipitated in a Ni-15Cr-8Fe-6Nb alloy, Metall. Mater. Trans. 29 (4) (1998) 1169–1174.
[46] H. Sugimura, Y. Kaneno, T. Takasugi, Alloying behavior of Ni3Nb, Mater. Trans. 51 (1) (2010) 72–77.
[47] A. Argon, Strengthening Mechanisms in Crystal Plasticity, Oxford University Press on Demand, 2008.
[48] Z. Wu, H. Bei, G.M. Pharr, E.P. George, Temperature dependence of the mechanical properties of equiatomic solid solution alloys with face-centered cubic crystal structures, Acta Mater. 81 (0) (2014) 428–441.
[49] J.M. Oblak, D.S. Duvall, D.F. Paulonis, An estimate of the strengthening arising from coherent, tetragonally-distorted particles, Mater. Sci. Eng. 13 (1) (1974) 51–56.
[50] T. Gladman, Precipitation hardening in metals, Mater. Sci. Technol. 15 (1) (1999) 30–36.
[51] S. Niu, H. Kou, T. Guo, Y. Zhang, J. Wang, J. Li, Strengthening of nano-precipitations in an annealed Al0.5CoCrFeNi high entropy alloy, Mater. Sci. Eng., A 671 (2016) 82–86.
[52] Y.-J. Chang, A.-C. Yeh, The formation of cellular precipitate and its effect on the tensile properties of a precipitation strengthened high entropy alloy, Mater. Chem. Phys. 210 (2018) 111–119.
[53] H.M. Daoud, A.M. Manzoni, N. Wanderka, U. Glatzel, High-temperature tensile strength of Al10Co25Cr8Fe15Ni36Ti6 compositionally complex alloy (High-Entropy alloy), JOM 67 (10) (2015) 2271–2277.
[54] A. Suzuki, M. Takeyama, Formation and morphology of Kurnakov type D022 compound in disordered face-centered cubic γ–(Ni, Fe) matrix alloys, J. Mater. Res. 21 (1) (2006) 21–26.
[55] R. Cozar, A. Pineau, Influence of the co/ni ratio on the γ and γ" precipitation in fe-ni-co-ta alloys, Metall. Trans. 5 (11) (1974) 2471–2472.
[56] S.E. Axter, D.H. Polonis, The influence of cobalt, iron and aluminum on the precipitation of metastable phases in the Ni-Ta system, Mater. Sci. Eng. 60 (2) (1983) 151–161.
[57] W.E. Quist, R. Taggart, D.H. Polonis, The influence of iron and aluminum on the precipitation of metastable Ni3Nb phases in the Ni-Nb system, Metall. Trans. 2 (3) (1971) 825–832.
[58] X. Gao, R. Hu, X. Li, G. Luo, Microstructure evolution during the precipitation and growth of fully coherent DO22 superlattice in an Ni-Cr-W alloy, Mater. Char. 118 (2016) 244–251.
[59] I. Kirman, D.H. Warrington, The precipitation of Ni3Nb phases in a Ni–Fe–Cr–Nb alloy, Metall. Trans. 1 (10) (1970) 2667–2675.
[60] X. Gao, R. Hu, G. Luo, The effect of Ti on precipitation of fully coherent DO22 superlattice in an Ni-Cr-W-based superalloy, Scripta Mater. 134 (2017) 15–19.
[61] R.C. Thomson, K.F. Russell, M.K. Miller, Phase separation in a Ni–37 at.% Co–5% Nb alloy, Mater. Sci. Eng., A 250 (1) (1998) 104–108.